Available online at www.sciencedirect.com
SCIENCE DIRECT®
Mechanics of Materials 35 (2003) 675–687
MECHANICS OF MATERIALS
www.elsevier.com/locate/mechmat

Using a micromechanical finite element parametric study to motivate a phenomenological macroscale model for void/crack nucleation in aluminum with a hard second phase

M.F. Horstemeyer *, S. Ramaswamy, M. Negrete

Center for Materials and Engineering Sciences, Sandia National Laboratories, P.O. Box 969, MS 9405, Livermore, CA, 94551-0969, USA

Received 2 January 2002; received in revised form 9 May 2002

Abstract

A multi-scale methodology that includes microscale finite element simulations, physical experiments, and a macroscale phenomenological model was used to determine the appropriate first-order influence parameters relating to void/crack nucleation. The finite element analyses were used to examine the role of seven independent features (number of silicon particle sites, uniformity of particle sizes which were micron size, shape of particles, additional microporosity, temperature, prestrain history, and loading conditions) in debonding and fracture of hard silicon particles in a cast A356 aluminum alloy. Owing to the wide range of features that can affect void/crack nucleation, an optimal matrix of finite element calculations is generated using a statistical method of design of experiments (DOE). The DOE method was used to independently screen the parametric influences concerning void/crack nucleation by second phase fracture or interface debonding. The results clearly show that the initial temperature was the most dominant influence parameter with respect to the others for both fracture and debonding. Experiments were then performed at three temperatures to quantify the void/crack nucleation from notch tensile specimen fracture surfaces. The data verified the importance of the temperature dependence on void/crack nucleation and showed that as the temperature decreased, the void nucleation rate increased. The Horstemeyer–Gokhale void/crack nucleation model was modified to include the temperature dependence and material constants were determined based on the experimental data. This study exemplifies a methodology of bridging various size scale analyses by sorting out the pertinent cause–effect relations from the structure–property relations.

1. Introduction

Certainly different methods can be used to derive constitutive equations related to void/crack nucleation (cf. Gurson, 1977; Horstemeyer and Gokhale, 1999), but a systematic methodology to include the most relevant features in a macroscale structure–property damage model has yet to be generated. This work was performed based on this premise. Our method starts with microscale finite element analysis in order to determine the pertinent influence parameters pertaining to void/crack nucleation that need to be captured in a

* Corresponding author. Tel.: +1-510-294-2816; fax: +1-510-294-1459.
E-mail address: mfhorst@sandia.gov (M.F. Horstemeyer).

0167-6636/03/$ - see front matter © 2002 Elsevier Science Ltd. All rights reserved.
doi:10.1016/S0167-6636(02)00165-5

macroscale continuum framework. So as not to confuse the reader, we use the term microscale, because the size of the silicon particles are microns in length. There is no inherent size scale parameter related to the constitutive model or to ABAQUS (Hibbitt et al., 1984), the finite element routine used in these studies. Experiments were then conducted to quantitatively confirm the microscale finite element results. Finally, the coupling of the microscale finite element results and experimental data are used to determine the macroscale continuum constitutive equation for void/crack nucleation.

No substantial effort thus far has gone into studying the relative roles played by simultaneously interacting microstructural and environmental features on second phase fracture and/or interface debonding. Developing a macroscale continuum model for void nucleation in a sense homogenizes discrete events, such as a fractured particle. Hence, one needs to include the first-order phenomenology from the cause–effect relations starting at the lower size scales. In a macroscale damage model, one cannot include all the degrees-of-freedom required from each discrete event. Consequently, all of the pertinent "effects" are to be captured, not all the "causes." The main focus of the micromechanical analyses is to qualify and, to a certain extent, quantify the influences of the interacting set of parameters on void nucleation events related to fracture or interface debonding.

For a cast A356 aluminum alloy, fracture of the main second phase (7% silicon) occurs simultaneously with aluminum–silicon interface debonding. Fig. 1 shows optical images of each type of damaging event.

The local stress/strain state in the region of the second phase is critical in determining if debonding or fracture occurs. Goods and Brown (1979) observed in several studies that equiaxed particles generally experience interface debonding while irregular shaped particles tend to fail by internal fracture. Needleman (1987, 1992) discussed the importance of the tensile hydrostatic stress that causes interface debonding. Dighe et al. (2002) also clearly shows the hydrostatic stress effects on debonding with experimental evidences related to the cast A356 aluminum alloy. For silicon fracture, Gall et al. (2000) performed atomistic simulations of aluminum–silicon interfaces and showed that defects and the maximum principle stress causes fracture of the second phase silicon.

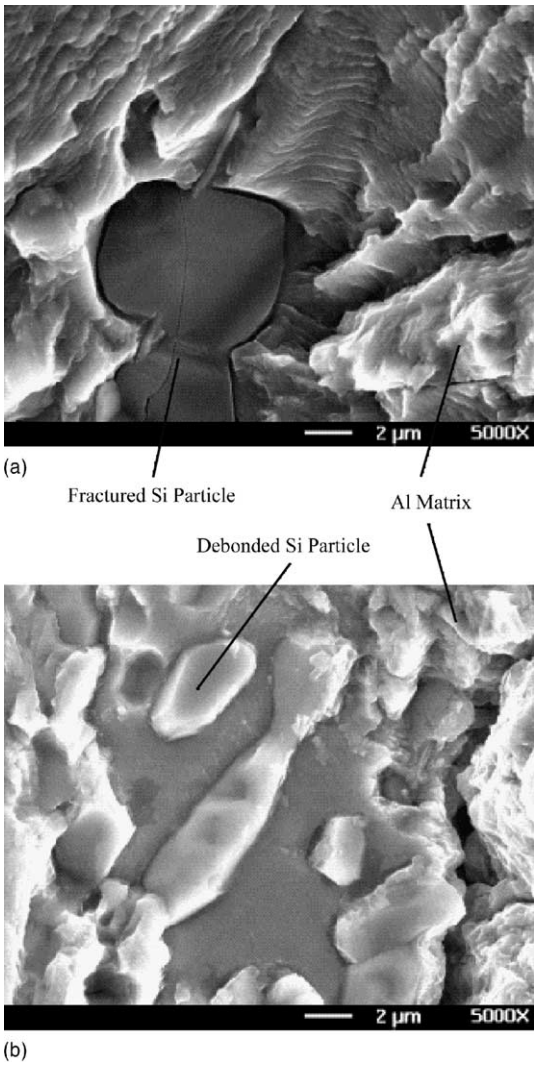

Fig. 1. Scanning electron microscope images of an A356 aluminum alloy showing (a) silicon particle fracture and (b) silicon–aluminum interface debonding.

Because we are considering seven parameters, a statistical procedure such as the DOE technique (Fisher, 1935a,b) makes sorting out the parametric effects efficient and clear. The DOE approach, popularized by Taguchi (1960, 1987) in the field of quality engineering, has recently been utilized in

various contexts of mechanics problems and design by Trinh and Gruda (1991), Horstemeyer (1993), Stutsman et al. (1996), Young (1996), Horstemeyer and McDowell (1997), and Horstemeyer and Ramaswamy (2000). The DOE methodology enables an investigator to select levels for each parameter and then conduct experiments in order to evaluate the effect of each parameter in an efficient manner. Any number of parameters and levels for each parameter can be placed in an orthogonal array, which lends itself to optimal determination of parametric effects. Here, orthogonality refers to the requirement that the parameters be statistically independent. The basic terminology of orthogonal arrays $L_a(b^c)$ is as follows: a denotes the number of calculations, b denotes the number of levels for each parameter and c denotes the number of parameters.

Eight finite element calculations under plane strain tensile conditions are performed on a cast A356 aluminum alloy using the plasticity model of Bammann et al. (1993, 1995). The DOE method is then used to screen the finite element results and yield the desired parametric influences on debonding and fracture of the silicon particles.

In our study, we seek to obtain the influences of seven independent parameters on two responses, namely, fracture of silicon particles and debonding of the aluminum matrix from the silicon particles, through micromechanical calculations. The following are the seven parameters adopted in our study: number of particles, size of particles, shape of particles, microporosity, temperature, prestain history, and loading direction. These seven parameters have been documented to significantly influence the mechanical response of materials. For our application, we were focused on a cast A356 aluminum alloy that was used for chassis components in automotive applications. As such, the bounding limits on the parameters were reasonably quantifiable as will be discussed.

The organization of this paper is as follows. The selection of the seven parameters considered in our study is described in detail in Section 2. Section 3 presents a brief overview of the DOE methodology. The constitutive model of Bammann et al. (1993, 1995) is described in Section 4. Section 5 presents the micromechanical results from the plane strain tensile finite element calculations along with the parametric influence results obtained through the DOE analysis. Section 6 discusses the experimental data, and Section 7 describes the macroscale void-crack nucleation model with temperature dependence.

2. Parameters

The parameters chosen for this study came about from many discussions with automotive component manufacturers. As such, the constraints on the levels come from experiences of the automotive industry and from information in the literature.

2.1. Number of silicon particles

Inclusions within metals are generally inhomogeneously present in various shapes, sizes and clusters throughout the material. The pattern of the inclusion distribution becomes important while considering nucleation in ductile metals. Some regions of the material could have regions with heavy concentrations of particles, while other regions may be relatively free of the inclusions. We examine the local interaction effects by keeping the nearest neighbor distance the same length, but we include the number of interacting particles as either two or four. Although the two parametric levels of two and four are arbitrary choices, these two types of clusters are often observed in the eutectic region of a cast A356 aluminum alloy.

2.2. Size of particles

Studies (Gurland, 1972; Dighe et al., 2002; Garrison and Moody, 1987) have shown that particles with greater sizes fail before smaller ones, unless clustering is present. This arises for potentially two reasons: the plastic strain increasing in the matrix material near a strong interface may not accommodate the large stresses experienced in the particle and/or the particle has more chances of flaws being present. The particle size in our study deals with the uniformity of the particle size with respect to the other sizes. We chose a uniform

distribution of sizes and a non-uniform distribution of particle sizes for our study. The relative size difference in the non-uniform distribution was 2:1.

2.3. Shape of particles

A more elongated shape of the second phase particle causes higher local stress concentrations over a more equiaxed shape. The relative importance though of this parameter compared to the number density or size is not clear. Two shapes were chosen, circular and elliptical. The elliptical particles have a major-to-minor axis ratio of 2:1. Certainly, other aspect ratios could have used in the study, but for a recent cast A356 al alloy, the aspect ratio of 2:1 was quantified by Dighe et al. (2000) and thus used in this study.

2.4. Microporosity

Tvergaard (1982), Tvergaard and Needleman (1995), and Horstemeyer and Ramaswamy (2000) showed that different levels of microporosity affected larger discrete pores in a deleterious manner with regard to void growth and coalescence. Microporosity in the context of this study means that a void volume fraction is given to a finite element. Hence, the size of the voids is below that of the particles. No large discrete voids are included in the microporosity level. By including microporosity in this study, we are examining the potential deleterious affects on the local stress/strain state such that void nucleation (silicon fracture or interface debonding) would be altered. Microporosity below a void volume fraction of 0.0001 is difficult to measure experimentally. Yet, levels of porosity lower than 0.0001 can occur in local regions influencing the resulting macro-mechanical properties. We used initial values of microporosity of zero and 0.000001 in this study.

2.5. Temperature

In Horstemeyer and Ramaswamy (2000) and Horstemeyer et al. (2000a,b), the initial temperature of the material was a first-order influence parameter on void coalescence via void impingement and the void-sheet mechanism. However, very little has been accomplished in the way of determining parametric effects on void nucleation at different temperatures. The temperature range chosen in this study is in the low homologous temperature range (294 and 400 K) to alleviate concerns about grain growth. Keep in mind that if the temperature levels used here were greater, the influence of the initial temperature on fracture and debonding would also be greater.

2.6. Prestrain history

Prestrain effects can arise from manufacturing processes where deformation-induced anisotropy is realized in a material or under conditions where non-monotonic loading sequences are experienced. MacKenzie et al. (1977) has shown from experimental data for several steels that, under rolling conditions, notch tensile tests are sensitive to the direction of loading. Horstemeyer and Revelli (1996) have also illustrated prestrain effects on void growth in several boundary value problems. A moderate prestrain level of 10% is chosen in this study to examine the history effects.

2.7. Loading direction

The loading direction is an influence parameter that plays an important role in determining the stress state of a material (Timoshenko and Goodier, 1970), which in turn has important consequences for void nucleation. In our plane strain finite element computations, the two directions of loading are chosen to be the horizontal direction and the vertical direction.

3. Design of experiments methodology

To handle seven interacting parameters in an efficient manner, we use the design of experiments (DOE) technique. The DOE method generates an optimal matrix (an orthogonal array) of finite element calculations suited for a set of parameters. Once the necessary finite element computations have been performed and the responses obtained, the DOE method is used as a screening process to obtain the desired parametric influences.

Each of the seven parameters is allowed to occupy one of two possible states during each calculation. The appropriate orthogonal array in our case is the $L_8(2^7)$, or simply L_8 array, which allows up to seven independent parameters with two levels for each parameter. Each level is characterized by a particular attribute. For example, the two levels for the temperature parameter are the end points of the temperature range of interest in a particular application (294 and 400 K). Although a full factorial set of calculations could be performed to vary each parameter in a linear fashion (the full set of calculations with seven parameters would be $2^7 = 128$), the DOE approach using an L_8 array requires only eight calculations. The advantage of DOE as a screening process for parameter influence grows exponentially as the number of parameter variations increases. Table 1 shows the L_8 array with the seven parameters and the two corresponding levels for each parameter.

In essence, the DOE method provides a linear system of equations that relates the responses $\{R\}$ from the finite element computations to the desired influences $\{A\}$ as

$$\{R\} = [P]\{A\}, \tag{1}$$

where $[P]$ is the parameter matrix corresponding to the chosen orthogonal array. The components of $\{R\}$, $\{A\}$, and $\{P\}$ are denoted by the following:

$$\{R\} = \begin{Bmatrix} R_1 \\ R_2 \\ R_3 \\ R_4 \\ R_5 \\ R_6 \\ R_7 \\ R_8 \end{Bmatrix}, \quad \{A\} = \begin{Bmatrix} 2A_0 \\ A_1 \\ A_2 \\ A_3 \\ A_4 \\ A_5 \\ A_6 \\ A_7 \end{Bmatrix},$$

$$[P] = \begin{bmatrix} +1 & +1 & -1 & -1 & -1 & -1 & +1 & +1 \\ +1 & +1 & -1 & -1 & +1 & +1 & -1 & -1 \\ +1 & +1 & +1 & +1 & -1 & -1 & -1 & -1 \\ +1 & +1 & +1 & +1 & +1 & +1 & +1 & +1 \\ +1 & -1 & -1 & +1 & -1 & +1 & -1 & +1 \\ +1 & -1 & -1 & +1 & +1 & -1 & +1 & -1 \\ +1 & -1 & +1 & -1 & -1 & +1 & +1 & +1 \\ +1 & -1 & +1 & -1 & +1 & -1 & -1 & -1 \end{bmatrix}. \tag{2}$$

The goal is to determine the values for $\{A\}$, given the DOE methodology provides $[P]$ and the finite element calculations give the response vector $\{R\}$. This is achieved by inverting the matrix $[P]$ in (1) to obtain

Table 1
DOEs simulation conditions and results

Calc	Loading	Size	Prestrain	Temperature	Distance	Shape	Initial microporosity	Fracture stress (MPa)	Debond pressure (MPa)
1	X (+)	Uniform (−)	$a_{xx} > 0$ $a_{yy} < 0$ (−)	294 K (−)	4 (+)	Round (−)	10E−6 (+)	667	329
2	Y (−)	Uniform (−)	$a_{xx} < 0$ $a_{yy} > 0$ (+)	400 K (+)	4 (+)	Round (−)	0 (−)	406	207
3	Y (−)	Uniform (−)	$a_{xx} > 0$ $a_{yy} < 0$ (−)	294 K (−)	2 (−)	Elliptic (+)	0 (−)	595	402
4	X (+)	Uniform (−)	$a_{xx} < 0$ $a_{yy} > 0$ (+)	400 K (+)	2 (−)	Elliptic (+)	10E−6 (+)	359	195
5	Y (−)	Non-uniform (+)	$a_{xx} > 0$ $a_{yy} < 0$ (−)	400 K (+)	4 (+)	Elliptic (+)	10E−6 (+)	413	250
6	X (+)	Non-uniform (+)	$a_{xx} < 0$ $a_{yy} > 0$ (+)	294 K (−)	4 (+)	Elliptic (+)	0 (−)	589	357
7	Y (−)	Non-uniform (+)	$a_{xx} > 0$ $a_{yy} < 0$ (−)	400 K (+)	2 (−)	Round (−)	0 (−)	344	195
8	X (+)	Non-uniform (+)	$a_{xx} < 0$ $a_{yy} > 0$ (+)	294 K (−)	2 (−)	Round (−)	10E−6 (+)	579	326

$$\{A\} = [P]^{-1}\{R\}. \tag{3}$$

As mentioned earlier, two sets of responses are considered in our study. They are nucleation by means of silicon particle fracture and by debonding of the aluminum–silicon interface. The quantities A_1, A_2, A_3, A_4, A_5, A_6 and A_7 reflect the influences of particle size, number of particles, particle shape, prestrain, temperature, additional microporosity, and loading direction, respectively.

The first column in the parameter matrix $[P]$ given in Eq. (2) relates to A_0, a statistical average of the DOE outputs. Except for column 1 in $[P]$, each level within any of the remaining columns occurs an equal number of times. This introduces the statistical independence, or balance, into the orthogonal array. If the response $\{R\}$ associated with one level changes at another level, then that parameter has a strong impact on the response being considered. Because different levels occur an equal number of times, an effect on the particular response of interest by each of the other parameters is canceled out. Hence, the positive and negative ones in matrix $[P]$ are simply used to express the effect of the two different levels.

4. Constitutive model

In this section we present a brief review of the temperature dependent viscoplastic model (Bammann et al., 1993, 1995) used in our calculations. This model involves three internal variables which include a second-order tensor variable $\underline{\boldsymbol{\alpha}}$ that represents the back stress which corresponds to kinematic hardening, a scalar variable κ that corresponds to isotropic hardening, and a microporosity, parameter $\boldsymbol{\phi}$. The evolution equations for $\underline{\boldsymbol{\alpha}}$ and κ are motivated from dislocation mechanics and are cast in a hardening-minus-recovery format accounting for both static and dynamic recovery. The evolution equation for the damage $\boldsymbol{\phi}$ is taken from the Cocks–Ashby model (Cocks and Ashby, 1980) of the growth of a spherical void in a viscoplastic material.

The model assumes an additive decomposition of the deformation rate and the spin tensor into elastic and plastic parts as

$$\underline{D} = \underline{D}^{\mathrm{e}} + \underline{D}^{\mathrm{p}}, \tag{4}$$

$$\underline{W} = \underline{W}^{\mathrm{e}} + \underline{W}^{\mathrm{p}}, \tag{5}$$

where D^{e} is expressed in terms of the stress rate as

$$\overset{\circ}{\underline{\boldsymbol{\sigma}}} = (1-\boldsymbol{\phi})\left[\left(K - \frac{2}{3}G\right)\mathrm{tr}(\underline{D}^{\mathrm{e}})\underline{\mathbf{I}} + 2G\underline{D}^{\mathrm{e}}\right] - \frac{\dot{\boldsymbol{\phi}}}{(1-\boldsymbol{\phi})}\underline{\boldsymbol{\sigma}}, \tag{6}$$

where K and G are the elastic bulk and shear moduli, respectively. $\underline{\mathbf{I}}$ is the second-order identity tensor, $\underline{\boldsymbol{\sigma}}$ is the Cauchy stress tensor, and $\overset{\circ}{\underline{\boldsymbol{\sigma}}}$ is the objective stress rate of a second-order tensor

$$\overset{\circ}{\underline{\boldsymbol{\sigma}}} = \dot{\underline{\boldsymbol{\sigma}}} - \underline{W}^{\mathrm{e}} \cdot \underline{\boldsymbol{\sigma}} + \underline{\boldsymbol{\sigma}} \cdot \underline{W}^{\mathrm{e}}. \tag{7}$$

Note that the damage $\boldsymbol{\phi}$ enters the elasticity equation in a manner that tends to degrade the elastic moduli. The plastic part $\underline{D}^{\mathrm{p}}$ is chosen to have strong nonlinear dependence on the deviatoric stress and is given by

$$\underline{D}^{\mathrm{p}} = \sqrt{\frac{3}{2}} f(\theta) \times \sinh\left[\frac{\sqrt{\frac{3}{2}}\|\underline{\xi}\| - (\kappa + Y(\theta))(1-\boldsymbol{\phi})}{V(\theta)(1-\boldsymbol{\phi})}\right] \frac{\underline{\xi}}{\|\underline{\xi}\|}, \tag{8}$$

where $\underline{\xi} \equiv \underline{\boldsymbol{\sigma}}' - (2/3)\underline{\boldsymbol{\alpha}}'$ is the (deviatoric) relative stress, and θ is the temperature. The expressions for the temperature-dependent yield functions $V(\theta)$, $Y(\theta)$, and $f(\theta)$ are defined as

$$V(\theta) = C_1 \mathrm{e}^{-C_2/\theta}, \tag{9}$$

$$Y(\theta) = C_3 \mathrm{e}^{C_4/\theta}, \tag{10}$$

$$f(\theta) = C_5 \mathrm{e}^{-C_6/\theta}, \tag{11}$$

where C_I $(I = 1, 6)$ are model parameters.

The evolution equations for the internal variables $\underline{\boldsymbol{\alpha}}$ and κ are stated in a hardening-minus-recovery format as

$$\overset{\circ}{\underline{\boldsymbol{\alpha}}} = h(\theta)\underline{D}^{\mathrm{p}} - \left[r_{\mathrm{d}}(\theta)\sqrt{\frac{2}{3}}\|\underline{D}^{\mathrm{p}}\| + r_{\mathrm{s}}(\theta)\right]\sqrt{\frac{2}{3}}\|\underline{\boldsymbol{\alpha}}\|\underline{\boldsymbol{\alpha}}, \tag{12}$$

$$\overset{\circ}{\kappa} = H(\theta)\sqrt{\frac{2}{3}}\|\underline{D}^{\mathrm{p}}\| - \left[R_{\mathrm{d}}(\theta)\sqrt{\frac{2}{3}}\|\underline{D}^{\mathrm{p}}\| + R_{\mathrm{s}}(\theta)\right]\kappa^2, \tag{13}$$

where the expressions for the temperature-dependent hardening (h and H), static recovery (r_{s} and R_{s}), and dynamic recovery (r_{d} and R_{d}) functions are defined as

$$r_{\mathrm{d}}(\theta) = C_7 \mathrm{e}^{-C_8/\theta}, \tag{14}$$

$$h(\theta) = C_9 \mathrm{e}^{-C_{10}/\theta}, \tag{15}$$

$$r_{\mathrm{s}}(\theta) = C_{11} \mathrm{e}^{-C_{12}/\theta}, \tag{16}$$

$$R_{\mathrm{d}}(\theta) = C_{13} \mathrm{e}^{-C_{14}/\theta}, \tag{17}$$

$$H(\theta) = C_{15} \mathrm{e}^{-C_{16}/\theta}, \tag{18}$$

$$R_{\mathrm{s}}(\theta) = C_{17} \mathrm{e}^{-C_{18}/\theta} \tag{19}$$

in which C_I $(I = 7, 18)$ are model parameters as well.

The evolution equation for the damage is given by

$$\dot{\boldsymbol{\phi}} = \boldsymbol{\beta}\left[\frac{1}{(1-\boldsymbol{\phi})^m} - (1-\boldsymbol{\phi})\right]\|\underline{D}^{\mathrm{p}}\|, \tag{20}$$

where $\boldsymbol{\beta}$ represents the triaxiality of the stress state and is expressed as

$$\boldsymbol{\beta} = \sinh\left[\frac{2(2m-1)p}{(2m+1)\boldsymbol{\chi}}\right], \tag{21}$$

with $p \equiv -\boldsymbol{\sigma}_{kk}/3$ and $\boldsymbol{\chi} \equiv \left(\boldsymbol{\sigma}'_{ij}\boldsymbol{\sigma}'_{ij}\right)^{1/2}$ being the pressure and effective stress, respectively, and m is a damage parameter related to void growth.

5. Micromechanical design of experiments results

The constitutive model outlined in the previous section is implemented using the ABAQUS general purpose finite element program (Hibbitt et al., 1984). One DOE analysis with eight calculations was performed under plane strain tensile loading conditions. The schematic representations of the geometries and boundary conditions for the calculations performed in the analysis are shown in Fig. 2. The initial void fraction just from the macroporosity was kept constant at 0.001 for all calculations performed. (Recall that microporosity was a parameter that added either 0.0 or 0.000001 distributed throughout the matrix to the total

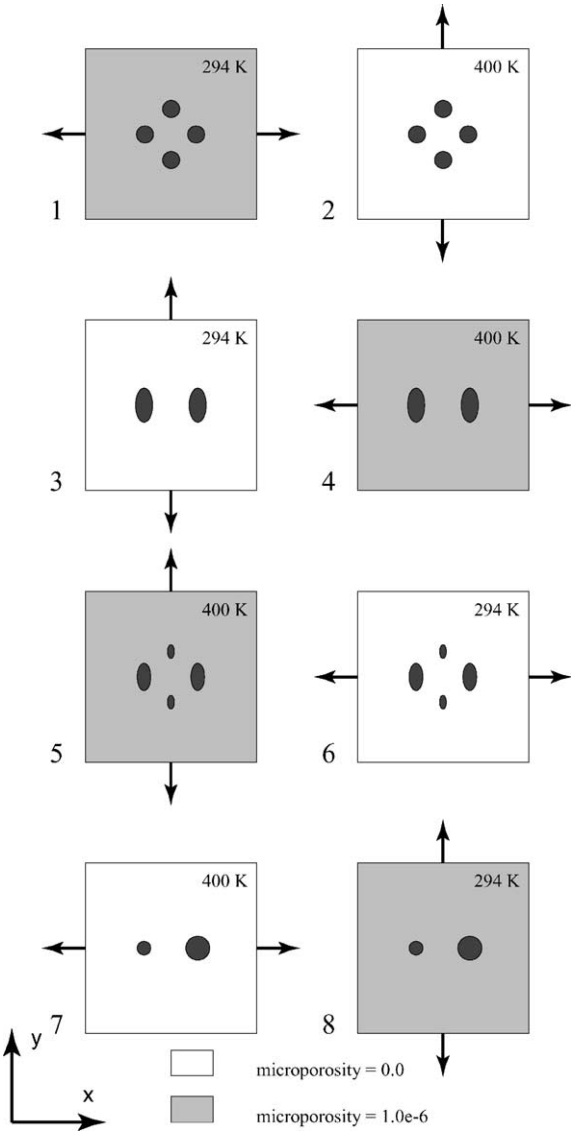

Fig. 2. Schematic illustrating geometries and loading conditions of the eight design of experiments numerical analyses. The parameters include temperature, particle size, particle shape, distribution, load direction, prestrain, and microporosity level.

porosity level.) The exterior boundaries of the undeformed configurations in each of the eight calculations were chosen to be unit squares. In our analysis we were interested in symmetric deformation modes and therefore analyze only one quadrant of the domain in calculations 1–6, and one half of the domain in calculations 7 and 8. Four-noded isoparametric plane strain elements with 2×2 Gauss integration points were used in the calculations. The determination of the material parameters C_I $(I = 1, \ldots, 18)$ and the damage parameter m is described in detail in Bammann et al. (1993, 1995). The values of these parameters for A356 aluminum are provided in the Appendix A.

The criterion used to determine fracture and interface debonding involved important assumptions. Because a wide variation of fracture stresses for silicon exists, we used a different approach than just appropriating a stress criterion. Instead, we ran the simulations all to the same applied (remote) strain level of 40%. Then, we determined the maximum principal stress within the silicon particle for each simulation. The peak principal stresses for each of the simulations were used to determine the relative parametric influence on fracture. A similar procedure was used to analyze interface debonding. Instead of the peak principle stress though, the negative pressure (tensile pressure) in the aluminum matrix adjacent to the silicon was used. Fig. 3 illustrates the distribution of principal stresses for the fracture case for simulation #4 as an example. Table 1 summarizes the DOE results for the fracture stresses and debonding pressures.

Figs. 4 and 5 show the normalized parametric influences on fracture and debonding, respectively, from the DOE analysis retrieved from the fracture stresses and debonding pressures shown in Table 1. Observe that the temperature is by far the most influential parameter in both cases. Although previous studies have shown the importance of the

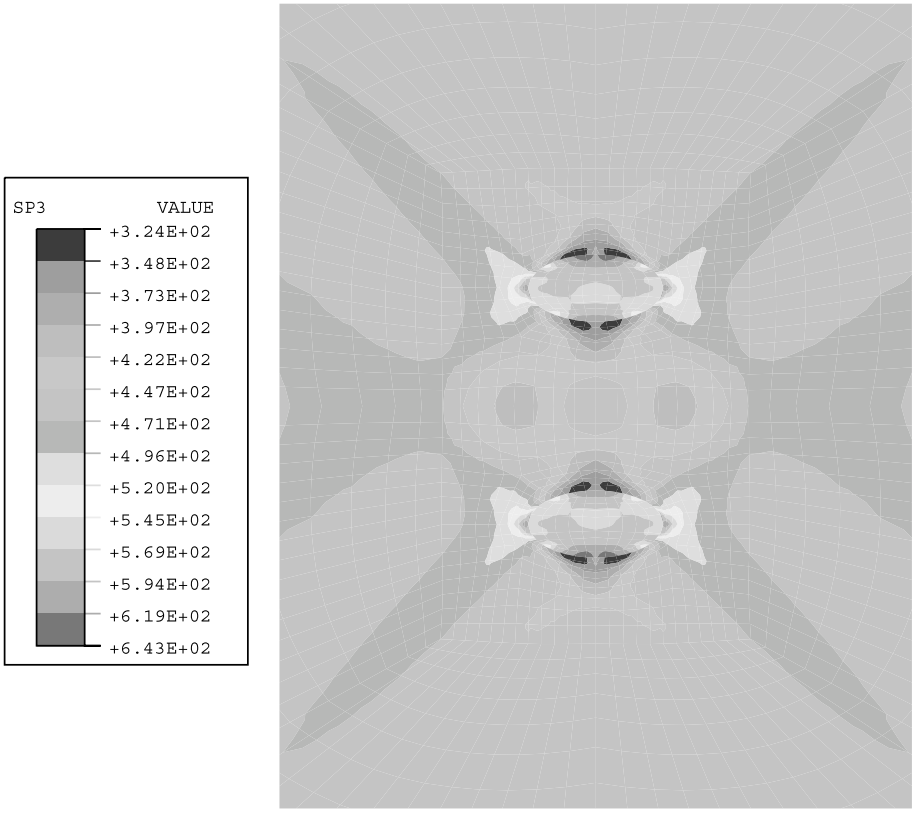

Fig. 3. Max principle stress contours (SP3 in MPa) for calculation #4 showing location of silicon particle fracture.

other parameters, no studies have revealed the relative importance of temperature over the other parameters with respect to the macroscale properties. The temperature differences cause higher mismatch stresses in the aluminum and silicon because their elastic moduli differ and the difference increases upon temperature changes. Furthermore, upon large local deformation the stress difference is exacerbated as the aluminum matrix experiences plastic deformation while the silicon experiences elastic deformation. When the temperature is changed in this case, the moduli mismatch is enhanced further.

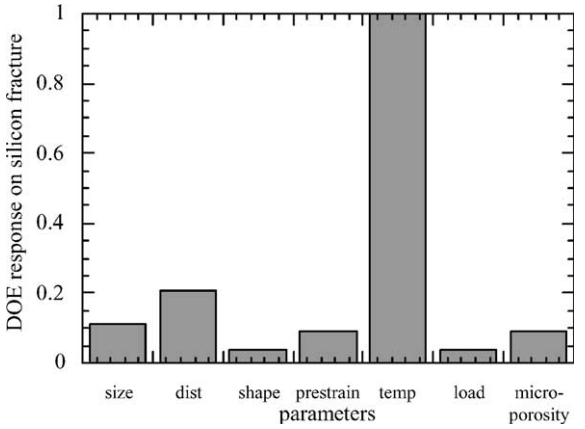

Fig. 4. Normalized DOEs results for void nucleation from silicon fracture.

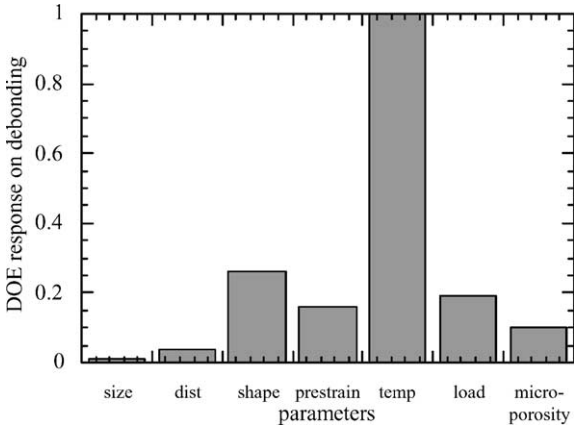

Fig. 5. Normalized DOEs results for void nucleation from silicon/aluminum debonding.

In analyzing the results, we note that the limits could, but might not, change the relative influence of a particular parameter, if the limits significantly differed from the ones chosen. For example, if a parameter other than temperature would have its range increased, it might be the greatest influence parameter. However, the values chosen were those quantified from the actual material from the actual automotive components. On the other hand, if a larger temperature range were chosen, the influence of temperature would still be the greatest as the study suggested, and no conclusions would change. As such, the qualitative trends of temperature difference giving the largest response difference is truly the most important parameter.

6. Experiments

The micromechanical parametric study indicated that temperature was the most dominant influence behavior for silicon fracture and aluminum–silicon interface debonding, and the other parameters were less important. As such, the next step in the methodology is to quantify the temperature effect by experiments. We performed notch tensile experiments (Bridgman, 1923) at different temperatures to measure the number density of fractured and debonds particles on the fracture surfaces. The specimens had a notch radius of 2.97 mm, and a specimen diameter of 9.525 mm. The remote strain rate was 0.01/s. The tests were performed at 222, 294, and 400 K. The tests were continued until fracture occurred. The fractured specimens were then sectioned and analyzed for silicon fracture and interface debonding (Gokhale et al., 1998). Fig. 6 shows that as the temperature increases, the number density of total fractured and debonded particles decreases. The same trend is observed when the area fraction (number fractured and debonded over the total number of particles) is used. The reason that the number density of fracture/debond sites increases at a lower temperature is that the local stress level and work hardening rate are higher at lower temperatures. These observations are in agreement with those of Yeh and Liu (1996), who varied the strength of an A357 alloy through heat treatment

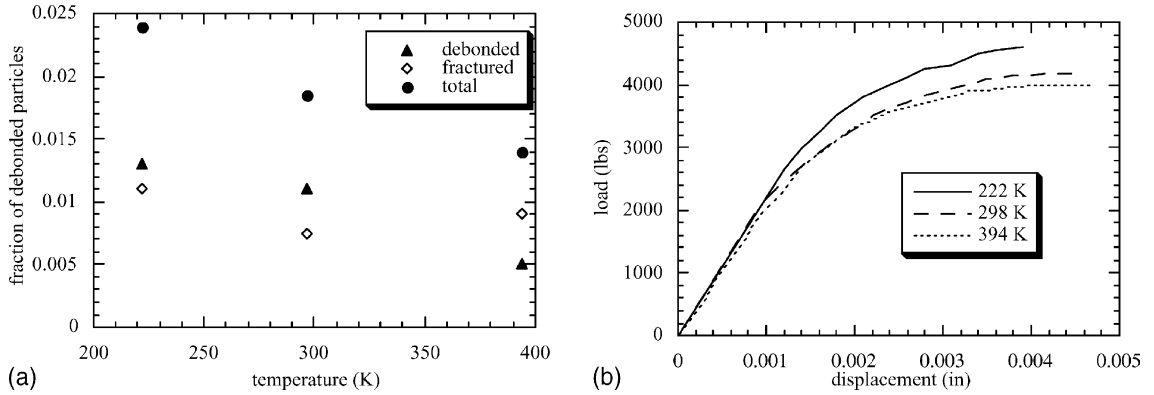

Fig. 6. (a) Number of damaged particles versus temperature and (b) corresponding load–displacement curves from notch tensile date.

and measured the fraction of broken silicon particles in the failed tensile test specimens. They observed at room temperature that the rate of fracture of silicon particles increases with the strength of the alloy. Note in Fig. 6b that the load–deflection response of the notch tensile tests reflect the damage nucleation experienced and revealed in Fig. 6a. For the colder temperature, the work hardening rate is higher but the elongation at failure is less. This correlates with a higher void/crack nucleation rate at colder temperatures. The trend continues to the hotter temperatures. The load-displacement curve shows a lower work hardening rate and higher elongation at failure, which correlates with the lower void/crack nucleation rate.

7. Macroscale modeling

Given that the microscale finite element parametric study and experimental data indicate an important temperature dependence on the void/crack nucleation, the void nucleation rule of Horstemeyer and Gokhale (1999) is modified by adding an exponential temperature dependence in the following manner,

$$\boldsymbol{\eta}(t) = C_{\text{coeff}} \exp\left(\frac{\boldsymbol{\varepsilon}(t) d^{1/2}}{K_{IC} f^{1/3}} \left\{ a \left[\frac{4}{27} - \frac{J_3^2}{J_2^3} \right] + b \frac{J_3}{J_2^{3/2}} + c \left\| \frac{I_1}{\sqrt{J_2}} \right\| \right\} \right) \exp\left(-\theta C_{T\boldsymbol{\eta}} \right), \quad (22)$$

where $\boldsymbol{\eta}(t)$ is the void nucleation density, $\boldsymbol{\varepsilon}(t)$ is the strain at time t, C_{coeff} is a material constant. θ is temperature in the absolute scale, and $C_{T\boldsymbol{\eta}}$ is the temperature dependent material constant determined from experiments (Fig. 6). An exponential function is used to fit to the data, which is shown in Fig. 7. The material parameters *a, b*, and *c* relate to the volume fraction of nucleation events arising from local microstresses in the material. These constants are determined experimentally from tension, compression, and torsion tests as discussed in Horstemeyer and Gokhale (1999) in which the number density of void/crack sites is measured at different strain levels. The stress state dependence on damage evolution is captured in Eq. (22) by using the stress invariants denoted by I_1, J_2, and J_3, respectively. I_1 is the first invariant of stress ($I_1 = \boldsymbol{\sigma}_{kk}$). J_2 is the second invariant of deviatoric stress ($J_2 = (1/2) S_{ij} S_{ij}$), where $S_{ij} = \sigma_{ij} - (1/3)\boldsymbol{\delta}_{ij}\boldsymbol{\sigma}_{kk}$. J_3 is the third invariant of deviatoric stress ($J_3 = S_{ij} S_{jk} S_{ki}$), The rationale and motivation for using these three invariants of stress is discussed in Horstemeyer and Gokhale (1999). The volume fraction of the second-phase material is *f*, the average silicon particle size is *d*, and the bulk fracture toughness is K_{IC}.

For the cast A356 aluminum alloy in our study, $K_{IC} = 17.3$ MPa m$^{0.5}$, $d = 6$ mm, and $f = 0.07$. The volume fraction and average size were determined from optical images of the sectioned test specimens. Fracture toughness tests were performed to determine K_{IC}. The stress state parameters were determined to be $a = 615.46$ GPa,

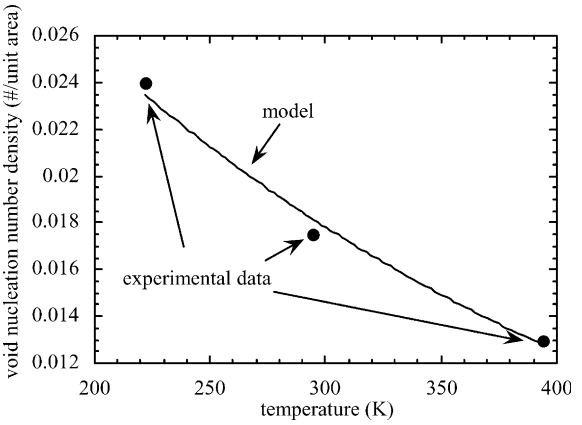

Fig. 7. Comparison of model to void nucleation data extracted from notch tensile tests performed at different temperatures.

$b = 58.64$ GPa, $c = 30.011$ GPa, and $C_{\text{coeff}} = 90$. In tension, compression, and torsion, specimens were strained to various levels and then unloaded. Samples from the specimens were extracted for image analysis, and the number of damaged sites were then counted.

Horstemeyer et al. (2000a,b) shows how the void/crack nucleation model, when coupled with void growth and coalescence imbedded in the BCJ plasticity model, is used within the context of solving boundary value problems. In the examples in Horstemeyer et al. (2000a,b) for notch tensile finite element simulations, one void/crack nucleation equation is assumed to capture both the silicon fracture and interface debonding effects. For consistency, $C_{T\eta}$ is determined from the addition of the silicon fracture and interface debonding sites as 0.009. If void nucleation were relegated to two separate equations, one for silicon fracture and one for interface debonding, $C_{T\eta}$ would need to be determined separately as well for each mechanism.

8. Summary

A multi-scale methodology that includes microscale finite element simulations, physical experiments, and a macroscale phenomenological model was used to determine the appropriate first-order influence parameters related to void/crack nucleation. The conclusions can be summarized by the three segments of this study:

1. A DOE technique was used to show the relative importance of second phase particle size, shape, and number density along with microporosity, temperature, prestrain history, and loading direction. This DOE analysis was performed in the context of microscale finite element simulations. The main result was that the second-phase fracture and debonding was mostly influenced by the initial temperature. All of the other parameters had a second-order influence on fracture and debonding.
2. Notch tensile experiments were then performed to quantify the temperature effects on void nucleation. Using optical methods, the number density of fractured and debonded particles were examined from specimens that were tested at three different temperatures (222, 294, 400 K). The experiments showed an Arrhenius temperature dependence on the number of fractured and debonded particles.
3. Because of the microscale results and experimental data, the Arrhenius temperature dependence on void nucleation was included in the Horstemeyer–Gokhale void/crack model. The model parameters were then determined from the experimental data. As such, the Horstemeyer–Gokhale void/crack nucleation model now has temperature dependence included with its stress state dependence, second particle size dependence, fracture toughness dependence, strain rate dependence, and volume fraction of second phase dependence.

Although this study focuses on a hard second-phase silicon particle in a softer aluminum matrix, the methodology of using a DOE study to help sort out the relative important parameters could be used for other material systems.

Acknowledgements

R.C. Osborne of General Motors Corporation and Don Penrod of the American Foundarymen's Society are recognized for their management of the

program. Support from the US Department of Energy, Sandia National Laboratories, under Contract DE-AC04-94AL85000 is gratefully acknowledged.

Appendix A

Material constants used for cast A356 aluminum alloy plasticity model.

E (GPa)	69.0
Poisson's ratio	0.33
Density (kg/m^3)	2700
C_1 (MPa)	0
C_2 (K)	0
C_3 (MPa)	3.768E+01
C_4 (K)	6.310E+02
C_5 (1/s)	1.000E+00
C_6 (K)	0
C_7 (1/MPa)	3.262E+01
C_8 (K)	1.434E+03
C_9 (MPa)	9.370E+02
C_{10} (K)	1.230E+00
C_{11} (s/MPa)	1.454E−03
C_{12} (K)	2.521E+02
C_{13} (1/MPa)	2.073E+05
C_{14} (K)	6.394E+03
C_{15} (MPa)	6.777E+01
C_{16} (K)	6.024E−02
C_{17} (s/MPa)	3.913E−03
C_{18} (K)	2.468E+03
C_{19}	1.700E−02
C_{20} (K)	7.700E+02

Note: base units in MPa, m, s, K.

References

Bammann, D.J., Chiesa, M.L., Horstemeyer, M.F., Weingarten, L.E., 1993. Failure in ductile materials using finite element methods. In: Jones, N., Wierzbicki, T. (Eds.), Structural Crashworthiness and Failure. Elsevier Applied Science, pp. 1–52.

Bammann, D.J., Chiesa, M.L., Johnson, G.C., 1995. A state variable damage model for temperature and strain rate dependent metal. In: Rajendran, A.M., Batra, R.C. (Eds.), Constitutive Laws: Theory, Experiments, and Numerical Implementation. CIMNE, Barcelona, pp. 84–97.

Bridgman, P.W., 1923. Compressibility of thirty metals as a function of pressure and temperature. Proc. Am. Acad. Arts Sci. 58 (5), 164–242.

Cocks, A.C.F., Ashby, M.F., 1980. Intergranular fracture during power law creep under multiaxial stresses. J. Met. Sci., 395–402.

Dighe, M.D., Gokhale, A.M., Horstemeyer, M.F., Mosher, D.A., 2000. Effect of strain rate effect on damage evolution in a cast Al–Si–Mg base alloy. Metall. Trans. 31A, 1725–1731.

Dighe, M.D., Gokhale, A.M., Horstemeyer, M.F., 2002. Second phase cracking and debonding observations in the fatigue damage evolution of a cast Al–Si–Mg alloy. Metall. Mater. Trans. 33A, 1–8.

Fisher, R.A., 1935a. Statistical Methods for Research Workers. Oliver and Boyd.

Fisher, R.A., 1935b. The Design of Experiments. Oliver and Boyd.

Gall, K., Horstemeyer, M.F., van Schilfegaarde, M., Baskes, M.I., 2000. Atomistic simulations on the tensile debonding of an aluminum–silicon interface. J. Mech. Phys. Solids 48, 2183–2212.

Garrison, W.M., Moody, N.R., 1987. Ductile fracture. J. Phys. Chem. Solids 48 (11), 1035–1074.

Gokhale, A.M., Dighe, M.D., Horstemeyer, M.F., 1998. Effect of temperature on silicon particle damage in A356 alloy. Metall. Mater. Trans. 29A, 905–908.

Goods, S.H., Brown, L.H., 1979. The nucleation of cavities by plastic deformation. Acta Metall. 27, 1–15.

Gurland, J., 1972. Acta Metall. 20, 735.

Gurson, A..L., 1977. Continuum theory of ductile rupture by void nucleation and growth: Part 1. Yield criteria and flow rules for porous ductile media. Trans ASME, J. Engng. Mater. Technol. 99, 2–15.

Hibbit, H.D. et al., 1984. ABAQUS/EPGEN—A general purpose finite element code with emphasis on nonlinear applications. Nucl. Engng. Des. 77, 271–297.

Horstemeyer, M.F., 1993. Structural analysis of a submarine using statistical design of experiments. In: Chen, E.P., Luk, V.K. (Eds.), Advances in Numerical Simulation Techniques for Penetration and Perforation of Solids, ASME-AMD-vol. 171, pp. 189–200.

Horstemeyer, M.F., McDowell, D.L., 1997. Using statistical design of experiments for parameter study of crystal plasticity modeling features under different strain paths. Sandia National Laboratory Report, SAND96-8683.

Horstemeyer, M.F., Revelli, V., 1996. Stress history dependent localization and failure using continuum damage mechanics concepts. In: McDowell, D. (Ed.), ASTM Symposium the Applications of Continuum Damage Mechanics to Fatigue and Fracture, STP1315.

Horstemeyer, M.F., Gokhale, A.M., 1999. A Void-crack nucleation model for ductile metals. Int. J. Solids Struct. 36, 5029–5055.

Horstemeyer, M.F., Lathrop, J., Gokhale, A.M., Dighe, M., 2000a. Modeling stress state dependent damage evolution in

a cast Al–Si–Mg aluminum alloy. Theor. Appl. Fract. Mech. 33, 31–47.

Horstemeyer, M.F., Ramaswamy, S., 2000. On factors affecting localization and void growth in ductile metals: a parametric study. Int. J. Damage Mech. 9, 6–28.

Horstemeyer, M.F., Matalanis, M.M., Sieber, A.M., Botos, M.L., 2000b. Micromechanical finite element calculations of temperature and void configuration effects on void growth and coalescence. Int. J. Plasticity 16, 979–1015.

MacKenzie, A.C., Hancock, J.W., Brown, D.K., 1977. On the influence of state of stress on ductile failure initiation in high strength steels. Engng. Fract. Mech. 9, 167–188.

Needleman, A., 1987. A continuum model for void nucleation by inclusion debonding. J. Appl. Mech. 109, 525–531.

Needleman, A., 1992. Micromechanical modeling of interfacial decohesion. Ultramicroscopy 40, 203–214.s.

Stutsman, R., Chamberlain, B., Evans, M., 1996. The design of an experiment to choose an aluminum die casting alloy for energy absorbing automotive components, SAE-SP-1164, no. 960159, pp. 1–7.

Taguchi, G., 1987. In: System of Experimental Design, vols. I and II. UNIPUB, New York.

Taguchi, G., 1960. Table of orthogonal arrays and linear graphs. Rep. Stat. Appl. Res., JUSE 6, 1–52.

Timoshenko, S.P., Goodier, J.N., 1970. Theory of Elasticity, third ed. McGraw-Hill Inc.

Tvergaard, V., 1982. Ductile fracture by cavity nucleation between larger voids. J. Mech. Phys. Solids 30 (4), 265–286.

Tvergaard, V., Needleman, A., 1995. Effects of nonlocal damage in porous plastic solids. Int. J. Solids Struct. 32 (8/9), 1063–1077.

Trinh, K.T., Gruda, J., 1991. Failure resistance of thin shells against projectile penetration. Sandia Report SAND91-8486, Sandia National Laboratories, Livermore, CA.

Yeh, J.W., Liu, W.P., 1996. Metall. Trans. A 27A, 3558–3568.

Young, S.H., 1996. An optimization technique using the finite element method and orthogonal arrays, Ph.D. thesis. Naval Postgraduate School, Monterey, CA.